OPEN ACCESS



The First Evidence of a Host Star Metallicity Cutoff in the Formation of Super-Earth Planets

Abstract

Planet formation is expected to be severely limited in disks of low metallicity, owing to both the small solid mass reservoir and the low-opacity accelerating the disk gas dissipation. While previous studies have found a weak correlation between the occurrence rates of small planets ($\lesssim 4R_{\oplus}$) and stellar metallicity, so far no studies have probed below the metallicity limit beyond which planet formation is predicted to be suppressed. Here, we constructed a large catalog of $\sim 110,000$ metal-poor stars observed by the TESS mission with spectroscopically derived metallicities, and systematically probed planet formation within the metal-poor regime ([Fe/H] ≤ -0.5) for the first time. Extrapolating known higher-metallicity trends for small, short-period planets predicts the discovery of ~ 68 super-Earths around these stars ($\sim 85,000$ stars) after accounting for survey completeness; however, we detect none. As a result, we have placed the most stringent upper limit on super-Earth occurrence rates around metal-poor stars ($-0.75 < [Fe/H] \leq -0.5$) to date, $\leq 1.67\%$, a statistically significant (p-value = 0.000685) deviation from the prediction of metallicity trends derived with Kepler and K2. We find a clear host star metallicity cliff for super-Earths that could indicate the threshold below which planets are unable to grow beyond an Earthmass at short orbital periods. This finding provides a crucial input to planet-formation theories, and has implications for the small planet inventory of the Galaxy and the galactic epoch at which the formation of small planets started.

Unified Astronomy Thesaurus concepts: Exoplanet astronomy (486)

1. Introduction

Under the core accretion paradigm, planet formation begins from the coagulation of solid material. Once this rocky core becomes massive enough (i.e., when its Bondi radius exceeds the core radius), gas accretion begins (e.g., Pollack et al. 1996), and the mass of the core ultimately determines the amount of accreted gas (e.g., Lee et al. 2014; Lee & Chiang 2015). This leads to the expectation of a strong correlation between the occurrence rate of gas giants and the amount of solid material in the disk, for which the metallicity of the host star is an excellent proxy (Johnson & Li 2012; Hasegawa & Hirashita 2014; Lee 2019). This giant planet-metallicity correlation has been well constrained from radial velocity surveys (Gonzalez et al. 2001; Fischer & Valenti 2005; Udry & Santos 2007; Johnson et al. 2010; Wang et al. 2015). On the other hand, the super-Earth-metallicity correlation is expected to be weaker

Original content from this work may be used under the terms of the Creative Commons Attribution 4.0 licence. Any further distribution of this work must maintain attribution to the author(s) and the title of the work, journal citation and DOI.

(Lee 2019), and indeed only emerges in the much larger sample available via the Kepler transit survey (Kutra et al. 2021; Lu et al. 2020; Zhu 2019; Petigura et al. 2018; Zink et al. 2023).

While the observed correlation is weak, there are many theoretical reasons to suggest that there may be a critical threshold metallicity below which the formation of super-Earths becomes difficult, if not impossible. A lower limit to metallicity could arise from the physics of dust grain-grain collisions and dust growth coupled with metallicity-dependent disk evolution (Johnson & Li 2012), instabilities believed to trigger planetesimal formation (Youdin & Goodman 2005; Johansen et al. 2007; Bai & Stone 2010; Squire & Hopkins 2018; Li & Youdin 2021), or the necessity for planetary protocores to accrete solids from their environment via planetesimal (Kokubo & Ida 1998; Goldreich et al. 2004) or pebble accretion (Ormel & Klahr 2010; Lambrechts & Johansen 2014; Lin et al. 2018). While the qualitative expectation of some threshold is generic to most models, actual predictions of where that threshold should lie vary significantly with values from 0.003 times solar metallicity (see Johnson & Li 2012; their Equation (10), evaluated at 0.1 au) to solar or supersolar metallicities (see Li & Youdin 2021, their Equation (14)) although the latter value is sensitive to the Stokes number of the coagulating dust grains (e.g., the critical minimum metallicity can be lower than the solar value if the Stokes number is large ~ 0.1).

¹¹ NSF Graduate Research Fellow.

¹² President's Postdoctoral Fellow.

¹³ NHFP Sagan Fellow.

Because of the well-studied stellar age–metallicity correlation in the Galaxy, the value of this critical metallicity threshold directly impacts when the earliest small planets were formed in the Galaxy—the oldest stars have metallicities significantly below the predicted range of values. Therefore, they would not be expected to form these planets. The super-Earth-metallicity correlation measured to date has been limited to host stars with metallicities greater than [Fe/H] = -0.4, due to the focus of Kepler on Sun-like stars, and the relative rarity of metal-poor stars in the local solar neighborhood.

To date, there has been no large, systematic search for small planets orbiting metal-poor host stars. However, the Transiting Exoplanet Survey Satellite (TESS; Ricker et al. 2015) enables consideration of the long-standing question: what is the critical metallicity required for small planet-core formation? Given that TESS is an all-sky survey providing high-precision photometry on millions of stars, the number of metal-poor stars surveyed is orders of magnitude greater than its predecessors, K2 and Kepler, enabling large population studies. Here, we perform the first analysis of the occurrence rates of small planets at metallicities approaching the predicted cut-offs for planet formation. We empirically test whether a metallicity cutoff exists and quantitatively address the metallicity below which such a drop in occurrence rate arises.

The outline of our paper is as follows: Section 2 provides a description of our stellar sample. In Section 3, we discuss our planet-detection pipeline. Section 4 contains a description of our forward model software. We discuss our results in Section 5. In Section 6, we compare our results to previous studies and their implications for super-Earth formation before summarizing our conclusions in Section 7.

2. Stellar Sample

Using the TESS Input Catalog (TIC; Ricker et al. 2015), we constructed a sample of metal-poor stars. We included TESS data from Sectors 1–55, and apply the following cuts.

- 1. Spectroscopically derived metallicities: the TIC compiled data from many surveys into a catalog of ~ 1.8 billion sources; thus, the spectroscopic metallicities are heterogeneous. The vast majority of these sources have parameters derived solely from photometric surveys, but the TIC also compiled data from the available spectroscopic surveys. To test existing planet formation theories, we included all stars with spectroscopically derived parameters having [Fe/H] < -0.5, hereafter known as the main sample. In addition, we included a subset of stars with metallicities between -0.5 and -0.25 to compare and cross-check our TESS planet-occurrence rates with previous results from Kepler and K2, referred to as the control sample hereafter. From this initial cut, we began with a main sample of 654,675 stars and control sample of 987,924 stars.
- 2. Stellar effective temperature: we limited our sample to stars with effective temperatures ranging from 4000–6500 K. This requirement selects FGK spectral types and allows for direct comparison with previous higher metallicity Kepler and K2 results. From this requirement, we excluded 32,609 main sample stars and 93,694 control sample stars.

- 3. Surface gravity: we excluded low-surface-gravity red giants by requiring $\log g > 4.0$ and removed 291,095 main sample stars and 377,648 control sample stars.
- 4. TESS magnitude ($T_{\rm mag}$): we selected stars brighter than $T_{\rm mag}=14$; at fainter magnitudes, our detection efficiency for small planets declines rapidly. From this cut, we excluded 232,312 main sample stars and 271,130 control sample stars.
- 5. Galactic Plane: we excluded stars with $|b| < 5^{\circ}$ to mitigate the effect of false positives due to crowding near the Galactic plane, removing 2265 main sample stars and 33,869 control sample stars.
- 6. Removal of Binary Stars: similar to previous works, we relied on the Gaia renormalized unit weight error (RUWE) metric to minimize this potential source of contamination and only included targets with RUWE<1.4 (Stassun & Torres 2021; Lindegren et al. 2018). Additionally, Gaia DR3 provides a flag, "non_single_star," which denotes sources that provide evidence of a binary (Creevey et al. 2023). Removing targets with Gaia binary flags and high RUWE values, we excluded 20,867 potential binary targets from that main sample and 31,429 from the control sample.

From these criteria, our main sample consisted of 75,527 metal-poor stars that are below $[Fe/H] \leqslant -0.5$ directly from the TIC. To increase the sample below $[Fe/H] \leqslant -0.5$ and better constrain the occurrence rate, we cross matched the TIC with LAMOST DR8 (Luo et al. 2015; the TIC is only complete to LAMOST DR3) to identify stars with spectroscopic parameters derived after the creation of the TIC. From LAMOST DR8, we gained an additional 9282 stars that pass our stellar sample cuts, resulting in a total of 84,809 metal-poor stars with metallicities below $[Fe/H] \leqslant -0.5$.

To enable a comparison with previous studies (e.g., Petigura et al. 2018; Zink et al. 2023), we also included a control sample of stars within the metallicity range of $-0.5 \le [Fe/H] \le -0.25$. In doing so, we account for any systematic difference between the combined Kepler and K2 occurrence rates and TESS. From the criteria listed above, our control sample consisted of 205,832 stars. Given the significant number of stars within this metallicity range, we included an additional cut to create our control sample, as the main objective of this study is to determine planet-occurrence rates below [Fe/H] = -0.5. We randomly selected 23,000 stars that produce a similar distribution of stellar properties as the metal-poor sample (see Figure 1). With the addition of the moderately more metal-rich subsample, our total sample included 107,809 metal-poor stars. In Table 1, we show the ranges and medians of the stellar properties for the total sample.

From the TIC, we found that approximately 90% of the stars within the final sample have metallicities from LAMOST, with the following surveys accounting for the remaining $\sim 10\%$: PASTEL (Soubiran et al. 2010), Hermes-TESS (Sharma et al. 2018), and Geneva-Copenhagen (Holmberg et al. 2009; see Figure 2). From these surveys, we determined the mean uncertainty for the metallicities to be ~ 0.04 dex. Given that the majority of the stars have metallicities derived from LAMOST spectroscopic data, the impact of systematic biases from other surveys is limited. However, for consistency, we transformed metallicities from PASTEL, Hermes-TESS, and Geneva-Copenhagen to LAMOST following the methodology in Soubiran et al. (2022). In brief, we determined the offsets

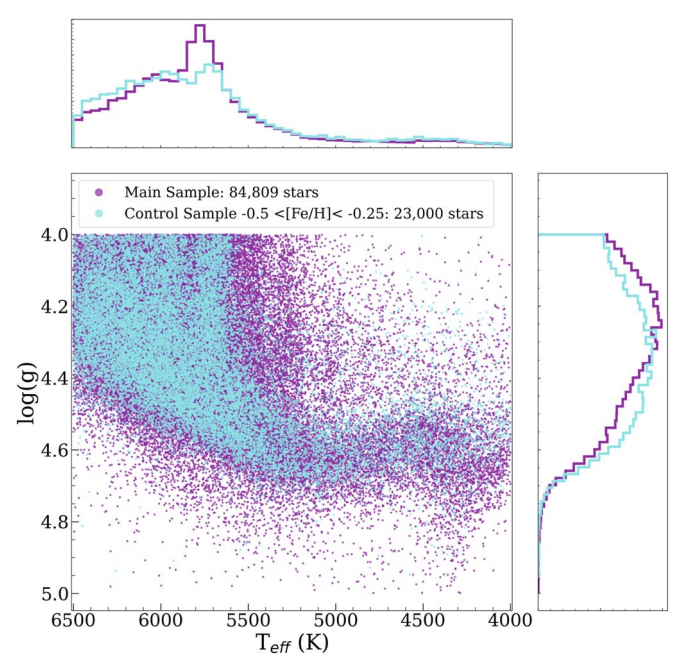


Figure 1. The stellar sample from TESS portrayed in the $T_{\rm eff}$ and log(g) plane. We show the main sample $(-1 \le {\rm [Fe/H]} \le -0.5)$ in purple, and the subsample $(-0.5 < {\rm [Fe/H]} \le -0.25)$ in blue.

Table 1
Stellar Sample Parameters: We Show the 5%–95% Quantiles for Each Paramete Range of Our Sample from the TIC (Stassun et al. 2018)

Parameter	Range	Median	Units
Mass	0.71-1.24	1.05	<i>M</i> _⊙
Radius	0.71 - 1.65	1.17	R_{\odot}
log(g)	4.04-4.63	4.31	cgs
TESS Magnitude	10.58-13.91	13.09	mag
Temperature	4646–6376	5819	K

between LAMOST and each survey using targets that overlap with LAMOST. We found the overlaps between LAMOST to be 102, 61, and 24 stars for PASTEL, Hermes-TESS, and Geneva-Copenhagen, respectively. A linear fit was produced using the offsets for each survey and LAMOST, and the [Fe/H] measurements were then calibrated to the LAMOST system using the linear fit. We found offsets to be 0.12, 0.07, and 0.09 dex for PASTEL, Hermes-TESS, and Geneva-Copenhagen, respectively.

In Figure 3, we show the stellar metallicities. The sharp peak at [Fe/H] = -0.5 is due to requiring spectroscopically derived metallicities $[Fe/H] \le -0.5$. Within the -0.25 to -0.5 bin, we note that the peak at approximately [Fe/H] = -0.4 results from the random cut performed when reducing the sample.

3. Planet Detection

While Boley et al. (2021) describes our planet-detection pipeline in detail, we briefly describe it here, noting additions and adjustments for this sample. For each star in our sample, we extract the light curves from TESS full-frame images. Before processing each light curve, we separated the data into the primary mission, 30 minute cadence observations (Sectors <27), and extended mission 1, 10 minute cadence (Sectors 27–55) observations. We do this to increase the detectability of planet candidates, as the primary and extended mission data do

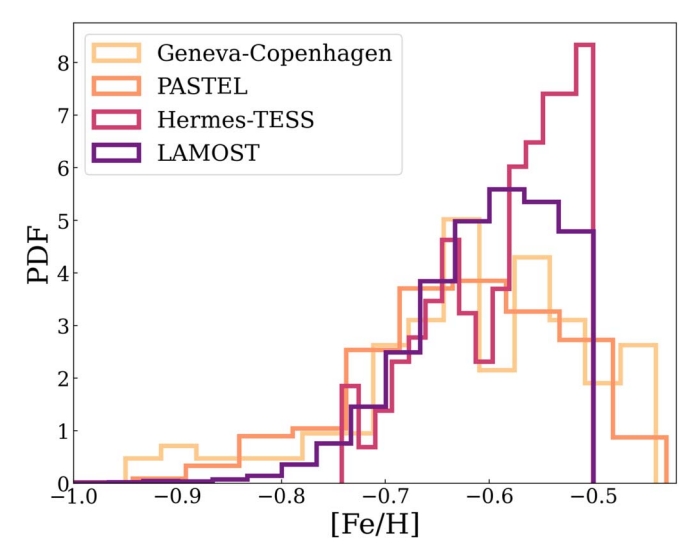


Figure 2. The probability density function (%) of the metallicities within our main sample $(-1 \le [Fe/H] \le -0.5)$ by survey. 90% of the stars within our sample have metallicities from LAMOST.

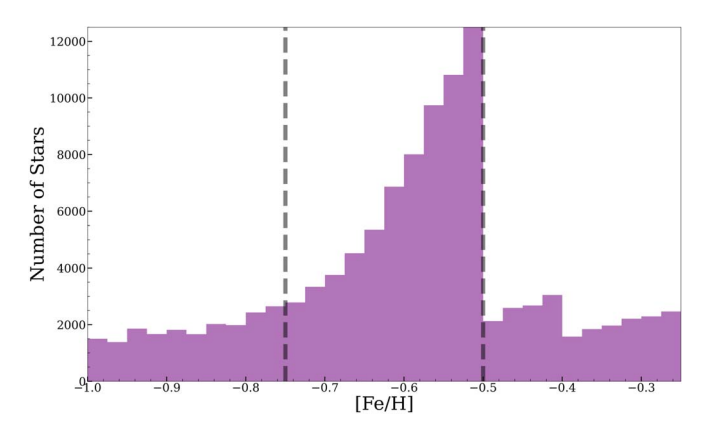


Figure 3. We show a histogram of the stellar metallicities for our sample with bins indicated by black dashed lines. The sharp peak at [Fe/H] = -0.5 is due to the reduction of the control sample as the main objective of this study is to determine super-Earth occurrence rates below [Fe/H] = -0.5.

not have the same noise levels or systematics. Given that the primary and extended mission data are separated, we preferentially chose the 10 minute cadence data when they were available for a given target. The primary mission data were processed for targets without extended mission data.

To optimize the light curves to be searched for planet candidates, we relied on the detrending software wotan (Hippke et al. 2019). Within wotan, we employed Tukey's biweight method, which is indicated to be the most robust detrending method (Hippke et al. 2019). Since the TESS data have sharp peaks at the beginning and ends of each observation sequence, we performed sigma-clipping to remove any systematics that wotan was unable to remove at the 5σ level.

We used transit least squares (TLS; Hippke & Heller 2019) as our transit search algorithm as it generally performs exceptionally well for smaller planets. Within TLS, we specified stellar mass, stellar radius, and limb-darkening coefficients, the latter of which were determined by interpolating the (Claret 2017) limb-darkening tables using the stellar effective temperature, surface gravity, and stellar metallicity from the TESS Input Catalog (Stassun et al. 2018). TLS produced a set of TCEs with a

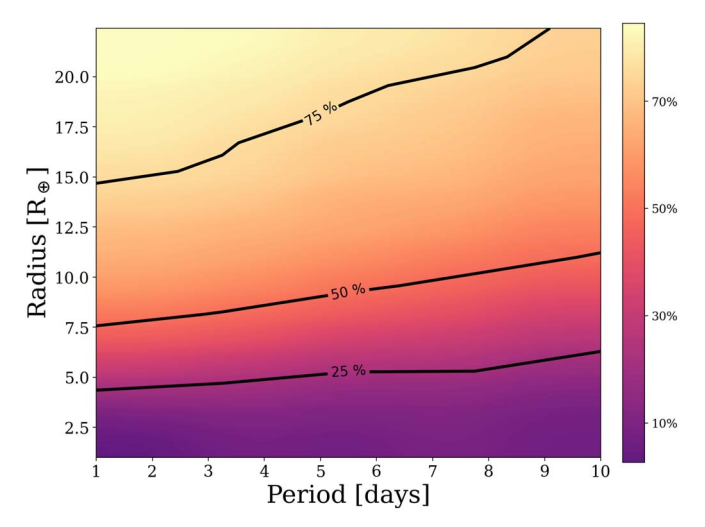


Figure 4. We show the detection efficiency of our pipeline, which is calculated via injection-recovery test. Purple indicates a lower detection efficiency, whereas yellow indicates a higher detection efficiency.

minimum of 3 transits that were then vetted and classified as planet candidates or false positives.

3.1. Survey Completeness

Using the framework in Boley et al. (2021), we conducted injection and recovery tests to determine the detection efficiency of our pipeline and vetting process. For each star in our sample, we uniformly sampled for periods between 1-10 days and radii between 1-3 R_{\oplus} . We choose to focus on periods between 1-10 days to ensure a one-to-one comparison with previous studies (Petigura et al. 2018; Zink et al. 2023). We assumed zero eccentricity, as planets on close-in orbits are subject to strong orbital circularization (Alvarado-Montes & García-Carmona 2019), and calculated limb-darkening coefficients as described above.

The simulated planets were injected into the light curves, which were then processed through our planet-detection pipeline described above. We considered a simulated planet successfully recovered if the signal-to-noise ratio was above 6σ , the false-alarm probability was ≤ 0.0001 , there were a minimum of three transits, and the period was within 1% of the injected period. Using the injection and recovery tests, a detection efficiency grid was created in orbital period and planet radius space, shown in Figure 4. The survey completeness was then calculated by multiplying the detection efficiency and the geometric transit probability, which is the ratio of the combined host star and planet radius to the planet's orbital radius

$$P_t(R_p, P) = \frac{R_p + R_{\star}}{a} \tag{1}$$

where R_{\star} is the stellar radius and a the orbital semimajor axis of the planet, determined from Kepler's third law.

4. Forward Model

Using the derived survey completeness, we can infer the intrinsic planet population by forward modeling. Given a population of planets, the forward model subjects the population to the selection effects of the detection pipeline, producing a simulated planet sample for comparison to the

observed sample. Following previous studies (Mulders et al. 2018; Zink et al. 2019, 2020b), our forward modeling followed the procedure.

- 1. Generate planet population: a synthetic planet population was generated using a joint power law in period-radius space and assigned a random orbital orientation.
- Determine detected planets: from the synthetic planet population, the number of transiting planets that would be observed by TESS was determined by simulating the instrumental and geometric selection effects.
- 3. Calculate planet population likelihood: using a modified Poisson likelihood (Zink et al. 2020b), the detectable planet population was compared to the observed planet candidates to determine the goodness of fit.
- Repeat: the likelihood continued to be drawn until the distribution of parameters was well sampled, typically 500,000 iterations.

To generate the planet population, we modeled the planet population-distribution function as a joint power law in planet radius (q(r)) and orbital period (g(p)) following the methodology outlined in (Zink et al. 2019). We assumed that the planet radius and orbital period distributions are independent, similar to previous studies, and modeled with broken power laws.

$$\frac{d^2N}{drdp} = fq(r)g(p) \tag{2}$$

$$q(r) \propto \begin{cases} r^{\alpha_1} & \text{if } r < R_{\text{br}} \\ r^{\alpha_2} & \text{if } r \geqslant R_{\text{br}} \end{cases}$$
 (3)

$$g(p) \propto \begin{cases} p^{\beta_1} & \text{if } p < P_{\text{br}} \\ p^{\beta_2} & \text{if } p \geqslant P_{\text{br}} \end{cases} \tag{4}$$

where f is the number of planets per star within our occurrence model, α_1 , α_2 , β_1 , and β_2 values are scaling model parameters. $P_{\rm br}$ and $R_{\rm br}$ represent the corresponding break in the period and radius power laws.

4.1. Model Optimization

Using the simulated planet populations, we measured the Bayesian posterior for the seven model parameters by employing the emcee affine-invariant sampler (Goodman & Weare 2010; Foreman-Mackey et al. 2013) with 50 semiindependent walkers, 5000 burn-in steps, and 10,000 sample steps. We used uniform priors for all scaling parameters. Specifically, the priors for α_1 , α_2 , β_1 , and β_2 range from -30 to +30. For $P_{\rm br}$, we only considered the range from 1–10 days similar to the range of our sample. For $R_{\rm br}$, the priors ranged from the minimum and maximum values for each planet type. Given the covariance in radius between super-Earths and sub-Neptunes, we separated these planet populations along the population valley (Fulton et al. 2017; Van Eylen et al. 2018). We used an empirically derived equation for the radius valley from Ho & Van Eylen (2023; Equation (4)):

$$\log_{10}\left(\frac{R_p}{R_{\oplus}}\right) = m \log_{10}\left(\frac{P}{\text{days}}\right) + c \tag{5}$$

where m = -0.11 and c = 0.37.

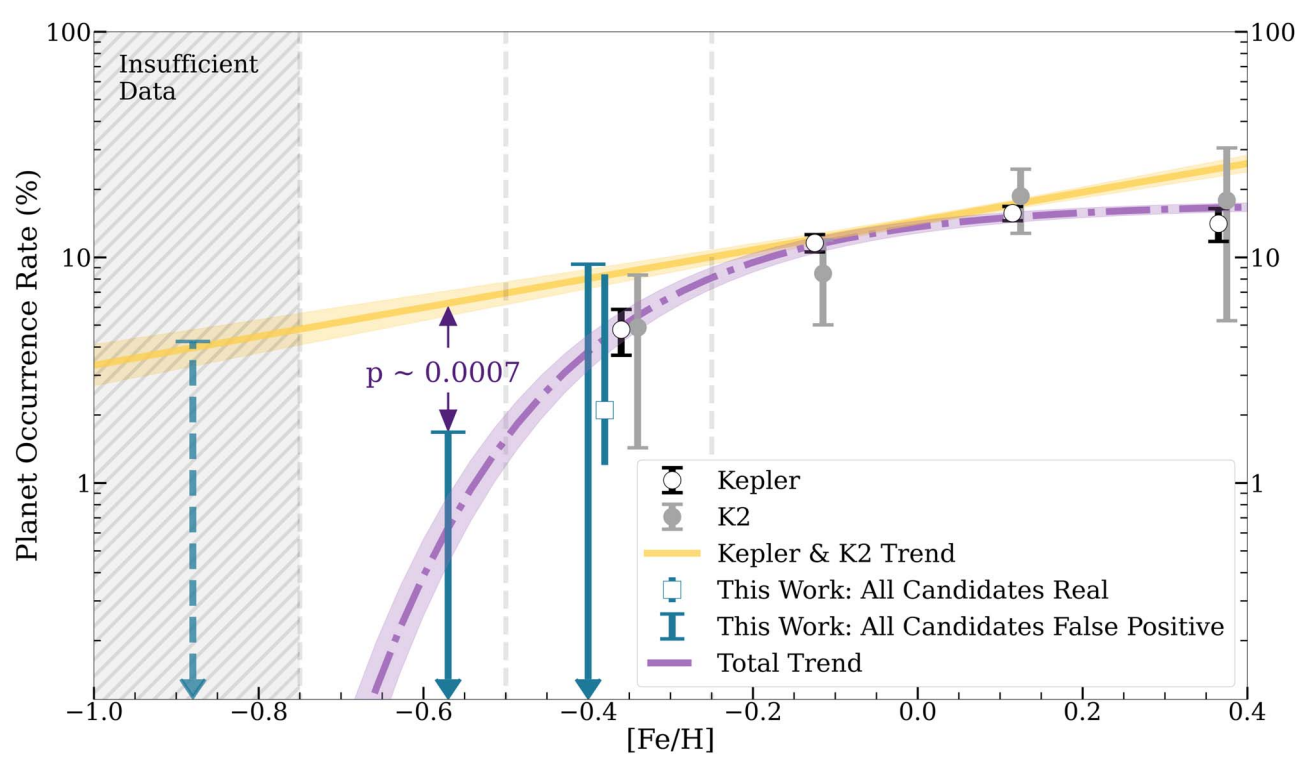


Figure 5. Super-Earth occurrence for Kepler (black circles) and K2 (gray circles), TESS data assuming all candidates are real (teal square), and 99.7% confidence intervals to calculate the upper limits for TESS data assuming all candidates are false positives (teal triangles) as a function of metallicity. The [-0.25, -0.5] bin occurrence rates are offset horizontally for visual clarity. The best-fit power-law trend line for the Kepler and K2 data (yellow) is displayed and extrapolated to [Fe/H] = -0.75 showing the 1σ uncertainties (Zink et al. 2023). We show the combined best-fit exponential trend line for Kepler, K2, and TESS (purple; Equation (6)) including the 1σ uncertainties. Each metallicity bin is indicated by gray dashed lines. Within the [-0.75, -1] bin, there is insufficient data to further constrain the super-Earth occurrence rate as a function of metallicity (denoted by the gray hatched region).

5. Results

Within our sample, we find a minimal increase in the detection efficiency as a function of metallicity. Stars at low metallicities are less active Amard & Matt (2020). They also have decreased opacities, resulting in smaller radii for a given temperature (Xin et al. 2022). Therefore, the difference in super-Earth detection efficiency between each metallicity bin ([-0.25, -0.5], [-0.5, -0.75], [-0.75, -1.0]) is $\sim 1\%$ on average, with the largest difference of 1.2% between the [-0.25, -0.5] and [-0.5, -0.75] bins. Therefore, the average detection efficiency being $\sim 10\%$ in the [-0.25, -0.5] bin would be $\sim 11.2\%$ in the [-0.5, -0.75].

Figure 5 displays the occurrence rates derived for our TESS sample, compared to previous analyses using Kepler and K2 (Zink et al. 2023). We analyzed the $-0.5 < [\text{Fe/H}] \le -0.25$ bin to overlap with those previous studies, to test for any systematic offsets from our TESS analysis. Within this bin, we found three planet candidates. We do not have any constraints on the false-positive rate (i.e., reliability) of our TESS planet candidates, so we test the most optimistic (all planet candidates are real) and conservative (all planet candidates are false positives) scenarios. Assuming all candidates are real, we find $f_{\text{real},[-0.25,-0.5]} = 2.1^{+6.6}_{-0.99}\%$, ¹⁴ consistent with the previous analyses. Assuming all the planet candidates are false positives, we place a 99.7% confidence interval upper limit of $f_{\bar{p},[-0.25,-0.5]} = 9.32\%$. Our result is consistent with previous studies, which find the occurrence rates to be $4.78 \pm 1.1\%$

 $4.88 \pm 3.45\%$ for Kepler and K2, respectively (Zink et al. 2023). Therefore, we do not find any statistically significant systematic offsets between TESS and the Kepler and K2 samples using our detection pipeline. Within the [-0.5, -0.75] bin, we detect no super-Earth candidates, and place a stringent 99.7% confidence interval upper limit of $f_{[-0.5, -0.75]} = 1.67\%$, shown in Figure 5.

Similarly, no super-Earth candidates are detected in the [-0.75, -1.0] bin. We find a 99.7% confidence interval upper limit of $f_{[-0.75,-1]} = 4.24\%$. However, given the limited sample size of 20,148 stars within this bin, we cannot further constrain super-Earth occurrence rate compared to Kepler and K2 extrapolations (Figure 5). To determine whether in super-Earth occurrence rate would continue to decrease in the [-0.75, -1.0] bin would require a sample \sim 4 times larger within that metallicity range based on our detection efficiency.

5.1. Exponential Fit

To determine an updated occurrence rate (f_p) trend as a function of metallicity, we combined the data from Kepler, K2, and TESS. We assume a simple exponential to model a cutoff in planet formation without introducing additional parameters above a power-law fit, of the form:

$$f_p = f_0 \exp\left[-10^{2([Fe/H]_{break} - [Fe/H])}\right]$$
 (6)

where f_0 is the initial occurrence rate at [Fe/H] = 0.4 and $[Fe/H]_{break}$ is the metallicity at which the slope of the exponential changes. To determine the best-fit parameters, we employed scipy.optimize.curve _fit. This software relies on a nonlinear least squares method to fit the exponential

The provided uncertainty is a direct measure of the 99.7% confidence interval from the sampled occurrence rate (f) posterior distribution.

(Vugrin et al. 2007). We find the best-fit parameters to be $f_0=17.33\pm0.7$ and $[{\rm Fe/H}]_{\rm break}=-0.31\pm0.02$ using 1σ uncertainties.

6. Discussion

A number of studies have considered planet-occurrence rates as a function of metallicity (see, e.g., Petigura et al. 2018; Johnson et al. 2010; Udry & Santos 2007; Fischer & Valenti 2005). Recently, Zink et al. 2023 used Kepler and K2 data to investigate the correlation between planet-occurrence rates and metallicities for short-period (1–10 days) planets from $1-20 R_{\oplus}$, directly comparable to our parameter space that also considers short-period planet on orbits of 1-10 days. Figure 5 shows their results for Kepler and K2, and an extrapolation of their combined trend from both data sets to lower metallicities. Below [Fe/H] ≤ -0.5 , the occurrence rate from the Kepler and K2 extrapolation combined with our measured survey completeness should yield a detection of 68 super-Earth candidates in our sample of TESS stars with a total of \sim 54 candidates in the [-0.5, -0.75] bin and ~ 14 candidates in the [-0.75, -1]. To calculate the expected value of super-Earth candidates within our below $[Fe/H] \leq -0.5$, we multiply the search completeness of our pipeline (\sim 1.4%) by the total sample (\sim 85,000 stars). We then multiply that value by the average extrapolated Kepler and K2 occurrence rate (\sim 5.7%) within that bin. Our new upper limit (1.67 %) is well below the extrapolated trend $(\sim 6.06\%)$ within the [-0.5, -0.75] bin, and is statistically discrepant with a p value = 0.000685. We calculate the p value by calculating the overlap of the TESS and Kepler and K2 distributions. Our pipeline has a detection threshold of 6σ , which is similar to detection thresholds used in previous TESS analyses (e.g., Thuillier et al. 2022; Ment & Charbonneau 2023). Adopting a considerably stricter requirement of 10σ for a TCE, reducing the parameter space in which we would detect signals but increasing the robustness of those signals, we find a lower but still strong discrepancy of with a p value = 0.0293. This is strong evidence that the trend in Zink et al. (2023) cannot be extended to lower metallicities, and that instead we are potentially seeing the onset of the expected critical metallicity cutoff for the formation of small planets.

This discovery has implications for planet formation. First, it represents an incredibly useful, observational constraint on models of planet formation. The critical metallicity threshold implied here may already be in tension with, or rule out, a number of proposed models. By comparing the dust settling timescale to the metallicity-dependent disk lifetime (e.g., Ercolano & Clarke 2010), Johnson & Li (2012) derived the critical metallicity required to have enough solid material in the disk midplane before the dispersal of the disk (see their Equation (10)). At the orbital distances relevant for our sample, their critical metallicity corresponds to [Fe/H] = -2.5, which is 2 orders of magnitude lower than our [Fe/H]_{break}. Population synthesis models that require initial core formation near the ice line and large-scale migration predict a range of critical metallicity for small planet formation from [Fe/H] > -1.8(Hasegawa & Hirashita 2014) to [Fe/H] > -0.6 (Andama et al. 2024), subject to disk parameters such as the level of turbulence. Similarly, using the pebble flux model of Lambrechts & Johansen (2014), Lin et al. (2018) computed the core mass growth as a function of disk turbulence and metallicity (see their Figures 15 an 16). We have repeated their calculation to find that the formation of an Earth-mass core becomes difficult subject to

disk turbulence when the metallicity falls below [Fe/H] \sim -0.7. From direct numerical simulations, Li & Youdin (2021) find the critical metallicity to trigger the initial clumping of solids via streaming instability to be sensitively determined by the particle Stokes number, the disk radial pressure gradient, and turbulence. A solar or subsolar critical metallicity would generally require a large Stokes number reaching \sim 0.1, which is near or above the maximum value expected in the analysis of nearby protoplanetary disks with concentric rings (e.g., Rosotti et al. 2020).

Second, it could imply that short-period super-Earths do not form early in the history of the universe. The vast majority of stars older than \sim 7 billion years, nearly half the lifetime of the Galaxy, have metallicities below -0.5 (Feuillet et al. 2019). If small planet formation must wait until the Galaxy has been enriched to a third of solar metallicity or more (Soubiran et al. 2008), after the death of the initial generations of stars enriching the interstellar medium (Abel et al. 2002; Beers & Christlieb 2005; Frebel et al. 2007; Clark et al. 2008), this threshold could directly inform the galactic inventory of small planets.

Extending our analysis to stars of even lower metallicities could improve our understanding of the nature of the metallicity cutoff. Even constructing a larger sample within the [-0.5, -0.75] bin within this study would be instrumental in providing a strong constraint on the critical metallicity for planet formation and perhaps constraining the properties of the protoplanetary disk. Therefore, subsequent studies at metallicities below [Fe/H] = -0.75 will reveal the complete picture of planet formation across Galactic space and time.

7. Summary and Conclusions

In this paper, we analyzed $\sim 110,000$ stars with spectroscopically derived metallicities within the metal-poor regime $(-1 \leqslant [Fe/H] \leqslant -0.25)$. The objective of this study was to detect super-Earths at periods of 1–10 days and determine their occurrence rates in order to test theoretical predictions of the critical metallicity threshold for small planet formation (Johnson & Li 2012; Lin et al. 2018; Li & Youdin 2021). From this study, we present our main conclusions:

- 1. We find a distinct metallicity "cliff" for super-Earths at low metallicities $(-0.75 \leqslant [Fe/H] \leqslant -0.5)$. This result suggests that super-Earths may be difficult to form within this regime, which, under certain disk conditions, is in line with formation theories that involve pebble accretion (e.g., Lin et al. 2018), planetesimal formation (e.g., Andama et al. 2024), and, more fundamentally, the initial solid clumping by streaming instability (e.g., Li & Youdin 2021; Section 5).
- 2. We find that planet-occurrence-rate trends above $[Fe/H] \gtrsim -0.5$ likely cannot be extended to more metal-poor environments (Section 5).
- 3. We provide a functional form for super-Earth occurrence rates as a function of metallicity (Equation (6), Section 5.1), and determine the metallicity cutoff to begin at [Fe/H]_{break} = -0.31 ± 0.02 using 1σ uncertainties.

Theory predicts that planet formation for all planet populations should become suppressed with decreasing metallicity (e.g., Johnson & Li 2012; Lee et al. 2014; Lee & Chiang 2015). However, this study is the first to discover empirical evidence suggesting that super-Earth formation may become significantly more difficult. Our study acts as an initial

investigation into super-Earth formation in the metal-poor regime, but more studies are necessary to determine whether this metallicity cutoff may be as steep for longer period planets. Given that metal-poor stars have shorter disk lifetimes and smaller disk masses (e.g., Yasui et al. 2010), long-period planet formation may be suppressed as well. However, transit studies with longer baselines would be required to probe the metallicity-correlation for longer period super-Earths. These observations will likely be feasible with Roman and PLATO launch in the coming decade.

Acknowledgments

We would like to thank Scott Gaudi for his insightful conversations and suggestions that have improved this work. K. M.B. acknowledges support from the NSF Graduate Research Fellowship Program under grant No. (DGE1343012). This research has made use of the NASA Exoplanet Archive, which is operated by the California Institute of Technology, under contract with the National Aeronautics and Space Administration under the Exoplanet Exploration Program. This paper includes data collected by the TESS mission. Funding for the TESS mission is provided by the NASA's Science Mission Directorate. The results reported herein benefited from collaborations and/or information exchange within NASAs Nexus for Exoplanet System Science (NExSS) research coordination network sponsored by NASA's Science Mission Directorate. This material is based upon work supported by the National Aeronautics and Space Administration under Agreement No. 80NSSC21K0593 for the program "Alien Earths." K.M.B. thanks the LSSTC Data Science Fellowship Program, which is funded by LSSTC, NSF Cybertraining grant No. 1829740, the Brinson Foundation, and the Moore Foundation; her participation in the program has benefited this work.

Software: emcee (Foreman-Mackey et al. 2013), eleanor (Feinstein et al. 2019), pylightcurve (Tsiaras et al. 2016), transit least quares algorithm (Hippke & Heller 2019), and astropy (Astropy Collaboration et al. 2013)

ORCID iDs

Kiersten M. Boley https://orcid.org/0000-0001-8153-639X Jessie L. Christiansen https://orcid.org/0000-0002-8035-4778 Jon Zink https://orcid.org/0000-0003-1848-2063 Kevin Hardegree-Ullman https://orcid.org/0000-0003-3702-0382

Eve J. Lee [®] https://orcid.org/0000-0002-1228-9820
Philip F. Hopkins [®] https://orcid.org/0000-0003-3729-1684
Ji Wang (王吉) [®] https://orcid.org/0000-0002-4361-8885
Rachel B. Fernandes [®] https://orcid.org/0000-0002-3853-7327
Galen J. Bergsten [®] https://orcid.org/0000-0003-4500-8850
Sakhee Bhure [®] https://orcid.org/0000-0002-6673-8206

References

```
Abel, T., Bryan, G. L., & Norman, M. L. 2002, Sci, 295, 93
Alvarado-Montes, J. A., & García-Carmona, C. 2019, MNRAS, 486, 3963
Amard, L., & Matt, S. P. 2020, ApJ, 889, 108
Andama, G., Mah, J., & Bitsch, B. 2024, A&A, 683, A118
Astropy Collaboration, Robitaille, T. P., Tollerud, J. E., et al. 2013, A&A, 558, A33
Bai, X.-N., & Stone, J. 2010, ApJ, 722, 1437
Beers, T. C., & Christlieb, N. 2005, AAR&A, 43, 531
Boley, K. M., Wang, J., Zinn, J. C., et al. 2021, AJ, 162, 85
Claret, A. 2017, A&A, 600, A30
```

```
Clark, P. C., Glover, S. C. O., & Klessen, R. S. 2008, ApJ, 672, 757
Creevey, O. L., Sordo, R., Pailler, F., et al. 2023, A&A, 674, A26
Endl, M., Cochran, W. D., Kürster, M., et al. 2006, ApJ, 649, 436
Ercolano, B., & Clarke, C. J. 2010, MNRAS, 402, 2735
Feinstein, A. D., Montet, B. T., Foreman-Mackey, D., et al. 2019, PASP, 131,
Feuillet, D. K., Frankel, N., Lind, K., et al. 2019, MNRAS, 489, 1742
Fischer, D. A., & Valenti, J. 2005, ApJ, 622, 1102
Foreman-Mackey, D., Hogg, D. W., Lang, D., & Goodman, J. 2013, PASP,
Frebel, A., Johnson, J. L., & Bromm, V. 2007, MNRAS, 380, L40
Fulton, B. J., Petigura, E. A., Howard, A. W., et al. 2017, AJ, 154, 109
Goldreich, P., Lithwick, Y., & Sari, R. 2004, ARA&A, 42, 549
Gonzalez, G., Laws, C., Tyagi, S., & Reddy, B. E. 2001, AJ, 121, 432
Goodman, J., & Weare, J. 2010, CAMCOS, 5, 65
Hasegawa, Y., & Hirashita, H. 2014, ApJ, 788, 62
Hippke, M., David, T. J., Mulders, G. D., & Heller, R. 2019, AJ,
Hippke, M., & Heller, R. 2019, A&A, 623, A39
Ho, C. S. K., & VanEylen, V. 2023, MNRAS, 519, 4056
Holmberg, J., Nordström, B., & Andersen, J. 2009, A&A, 501, 941
Johansen, A., Oishi, J. S., Mac Low, M.-M., et al. 2007, Natur,
   448, 1022
Johnson, J. A., Aller, K. M., Howard, A. W., & Crepp, J. R. 2010, PASP,
   122, 905
Johnson, J. L., & Li, H. 2012, ApJ, 751, 81
Kokubo, E., & Ida, S. 1998, Icar, 131, 171
Kutra, T., Wu, Y., & Qian, Y. 2021, AJ, 162, 69
Lambrechts, M., & Johansen, A. 2014, A&A, 572, A107
Lee, E. J. 2019, ApJ, 878, 36
Lee, E. J., & Chiang, E. 2015, ApJ, 811, 41
Lee, E. J., Chiang, E., & Ormel, C. W. 2014, ApJ, 797, 95
Li, R., & Youdin, A. N. 2021, ApJ, 919, 107
Lin, J. W., Lee, E. J., & Chiang, E. 2018, MNRAS, 480, 4338
Lindegren, L., Hernández, J., Bombrun, A., et al. 2018, A&A, 616, A2
Lodders, K. 2010, Principles and Perspectives in Cosmochemistry (Berlin:
   Springer-Verlag), 379
Lu, C. X., Schlaufman, K. C., & Cheng, S. 2020, AJ, 160, 253
Luo, A. L., Zhao, Y.-H., Zhao, G., et al. 2015, RAA, 15, 1095
Marcy, G., Butler, R. P., Fischer, D., et al. 2005, PThPS, 158, 24
Masuda, K., & Winn, J. N. 2017, AJ, 153, 187
Mayor, M., Marmier, M., Lovis, C., et al. 2011, arXiv:1109.2497
McCarthy, C., & Zuckerman, B. 2004, AJ, 127, 2871
Ment, K., & Charbonneau, D. 2023, AJ, 165, 265
Miller, N., & Fortney, J. J. 2011, ApJL, 736, L29
Moe, M., & Kratter, K. M. 2019, arXiv:1912.01699
Moe, M., Kratter, K. M., & Badenes, C. 2019, ApJ, 875, 61
Mortier, A., Santos, N. C., Sousa, S., et al. 2013, A&A, 551, A112
Mortier, A., Santos, N. C., Sozzetti, A., et al. 2012, A&A, 543, A45
Mulders, G. D., Pascucci, I., Apai, D., & Ciesla, F. J. 2018, AJ, 156,
Ormel, C. W., & Klahr, H. H. 2010, A&A, 520, A43
Petigura, E. A., Marcy, G. W., Winn, J. N., et al. 2018, AJ, 155, 89
Pollack, J. B., Hubickyj, O., Bodenheimer, P., et al. 1996, Icar, 124, 62
Rosotti, G. P., Teague, R., Dullemond, C., Booth, R. A., & Clarke, C. J. 2020,
         S. 495, 173
Ricker, G. R., Winn, J. N., Vanderspek, R., et al. 2015, JATIS, 1, 014003
Sharma, S., Stello, D., Buder, S., et al. 2018, MNRAS, 473, 2004
Soubiran, C., Bienaymé, O., Mishenina, T. V., & Kovtyukh, V. V. 2008, A&A,
Soubiran, C., Brouillet, N., & Casamiquela, L. 2022, A&A, 663, A4
Soubiran, C., Le Campion, J. F., Cayrel de Strobel, G., & Caillo, A. 2010,
   A&A, 515, A111
Squire, J., & Hopkins, P. F. 2018, MNRAS, 477, 5011
Stassun, K. G., & Torres, G. 2021, ApJL, 907, L33
Stassun, K. G., Oelkers, R. J., Pepper, J., et al. 2018, AJ, 156, 102
Thuillier, A., Van Grootel, V., Dévora-Pajares, M., et al. 2022, A&A,
   664, A113
Tsiaras, A., Waldmann, I. P., Rocchetto, M., et al. 2016, pylightcurve:
   Exoplanet lightcurve model, Astrophysics Source Code Library,
   ascl:1612.018
Udry, S., & Santos, N. C. 2007, ARA&A, 45, 397
Van Eylen, V., Agentoft, C., Lundkvist, M. S., et al. 2018, MNRAS, 479,
Vugrin, K. W., Swiler, L. P., Roberts, R. M., Stucky-Mack, N. J., &
```

Sullivan, S. P. 2007, WRR, 43, W03423

```
Wang, J., Fischer, D. A., Horch, E. P., & Huang, X. 2015, ApJ, 799, 229
```

Xin, C., Renzo, M., & Metzger, B. D. 2022, MNRAS, 516, 5816
Yasui, C., Kobayashi, N., Tokunaga, A. T., Saito, M., & Tokoku, C. 2010, ApJL, 723, L113

Youdin, A. N., & Goodman, J. 2005, ApJ, 620, 459

Zhu, W. 2019, ApJ, 873, 8

Zink, J. K., Christiansen, J. L., & Hansen, B. M. S. 2019, MNRAS, 483, 4479Zink, J. K., Hardegree-Ullman, K. K., Christiansen, J. L., et al. 2020b, AJ, 160, 94

Zink, J. K., Hardegree-Ullman, K. K., Christiansen, J. L., et al. 2023, AJ, 165, 262